Supplementary Information for

Got Coke? Self-Limiting Poisoning Makes an Ultra Stable and Selective Sub-nano Cluster Catalyst

Guangjing Li[†], Patricia Poths[†], Tsugunosuke Masubuchi, Harry W. T. Morgan, Anastassia N. Alexandrova[*], Scott L. Anderson[*]

[†]These authors contributed equally to this work.
[*]Correspondence to: ana@chem.ucla.edu, anderson@chem.utah.edu

This PDF file includes:

Supplementary Text
Figs. S1 to S10
Tables S1 to S2
References

TEM images of Pt_4 clusters

Scanning TEM in high angle annular dark field mode was used to image several sizes of Pt_n clusters deposited on Au supported ultra-thin carbon films, as shown in Fig. S1. For the XPS, ISS, and TPD experiments, the alumina deposition substrates were positioned ≤0.5 mm behind a 2 mm diameter deposition mask, thus the measured cluster currents only include clusters depositing on the alumina substrate, in a cluster spot close to 2 mm diameter. For imaging, deposition was done at the same ~1 eV/atom energy, but the TEM grid holder did not allow the grids to be positioned immediately behind the deposition mask, and we estimate that only ~0.85% of the cluster beam current corresponds to clusters depositing on the grid.

Fig. S1A shows an image of Pt_{10} clusters on an ultra-thin carbon film, and Fig. S1B shows the ImageJ analysis, which counted 133 cluster spots, with mean diameter of 0.82 nm. The analysis has significant uncertainty due to the substantial contrast variation from the carbon grid; nonetheless, the spot density is nearly identical to the density predicted from the estimated coverage (131 clusters in the analysis area). Furthermore, the cluster spots were found to be stable in both position and contrast in repeated images. Both the spot stability under the e-beam and the spot density, suggest that the Pt_{10} clusters were stable with respect to diffusion, agglomeration, and ripening. Fig. S1C shows a higher magnification image of Pt_{10} clusters deposited on a ~31 nm thick oxidized aluminum film, which should better represent the behavior on the alumina/Ta (110) substrate used in the XPS, ISS, and TPD experiments. Here too, the spots were present with density close to that predicted from the estimated deposition density, and were stable under the e-beam, suggesting that Pt_{10}/alumina is reasonably stable with respect to sintering.

The final image in Fig. S1D is for Pt_4 deposited on an ultrathin carbon film at 0.01 ML-equivalent coverage. As expected, the cluster spots were smaller, with lower contrast compared to Pt_{10}/carbon, and again were stable under the e-beam, however, in this case the number of clearly identifiable spots was more than an order of magnitude smaller than expected from the estimated deposition density. We attribute the discrepancy most to the difficulty of distinguishing cluster spots from contrast variations in the carbon film. The small spot density might be taken as evidence that the Pt_4 clusters were sintering to produce a smaller number of larger clusters, however, but in this we would expect to see much higher spot contrast. To explain ten times fewer-than-expected spots, the average sintered Pt_n cluster would contain more than 40 atoms, and therefore would appear brighter and larger than the Pt_{10} clusters in Fig. S1A. We conclude from the absence of large, high contrast spots, that the Pt_4/carbon clusters are also stable, but were simply lost within the contrast variation of the carbon film.

Desorption during the first heating of Pt_4Ge/alumina: Removing HCl and absence of C_2D_4 binding to the clusters

The Pt_4Ge/alumina samples as prepared, prior to any heating, still had some Cl atoms on the surface, and the clusters were saturated with hydrogen. Therefore, the final step in the preparation process was to heat the samples to drive off Cl and H, and the desorption was shown in Fig. S2. The sample was cooled to 150 K and exposed to 10 L of C_2D_4, which we added as probe of exposed cluster binding sites. The sample was then heated at 3 K/sec to 750 K while monitoring C_2D_4, D_2, $H^{35}Cl$, and $^{35}Cl_2$ desorption. Cl_2 desorption was not observed, so data are shown only for C_2D_4, D_2, $H^{35}Cl$. C_2D_4 desorbed at low temperatures, associated with C_2D_4 desorption from the support, with no desorption at higher temperatures, associated with cluster binding sites. Clearly the clusters were saturated with Cl and H do that C_2D_4 adsorbed only on

the support. No D_2 desorption (or carbon deposition) was observed – further evidence (cf. Fig. 2) that C_2D_4 does not dehydrogenate on the Ge/alumina support. HCl desorption began as soon as the sample was heated above the 300 K temperature used for the $GeCl_4$ and H_2 doses in the Ge deposition treatment. The inset also shows that there was no HCl desorption in 2nd and 3rd heatings (5 were tested), indicating that no Cl remained on the surface after the first heating.

TPD quantification

As described above, we calibrated the relationship between the number of molecules desorbing from the surface and the ion counts measured by the mass spectrometer during TPD. The data shown in Fig. 2 of the main paper have been corrected to molecules desorbing using the calibration process, and the TPD curves were then integrated to obtain the total numbers of molecules desorbing in each TPD cycle. The integrated numbers of molecules desorbing are shown in Tables S1 and S2, for the first 6 TPD cycles on Pt_4/alumina and Pt_4Ge/alumina. In later cycles the signals for D_2 are small enough that uncertainties due to correction for mass spectrometer background makes them unreliable. It should be noted that there are also uncertainties relating to how the (unknown) desorption angular distributions affect detection efficiencies, and how the detection efficiency of the mass spectrometer varies with the distance of the desorption site from axis of the mass spectrometer. It is difficult to quantify either of these uncertainties, and we, therefore, assign a rather large ±50% uncertainty to the values in the tables.

Integrated desorption values are given in terms of numbers of C_2D_4 or D_2 molecules desorbing *per* Pt atom on the surface, and in terms of molecules/cluster. This is possible because we know quite precisely how many clusters were deposited in the analysis area. For Pt_4 clusters, the 0.1 ML equivalent coverage translates to 1.18×10^{12} clusters or 4.71×10^{12} atoms in the

cluster spot, all of which are visible to the TPD mass spectrometer. As shown in Fig. 2, some molecules also desorb from the Pt-free alumina and Ge/alumina supports, and those integrated values are given in the "alumina" and "Ge/alumina" lines in the table. To allow direct comparison with the results for the cluster-containing samples, they also have been normalized to the numbers of Pt atoms or clusters are present in the cluster-containing samples. The desorbing molecule values for the cluster-containing samples have been corrected by subtracting the alumina and Ge/alumina values. The total number of C_2D_4 molecules adsorbed during the 150 K dose starting each TPD cycle was estimated assuming that only carbon was left on the surface at 750 K. In that case, total C_2D_4 adsorbed = C_2D_4 desorbing + 0.5*D_2 desorbing.

XPS quantification

The Ge:Pt coverage ratio prepared by the $GeCl_4/H_2$/heating process used to prepare Pt_4Ge/alumina was estimated from the ratio of Ge 2p and Pt 4d XPS intensities. Because the deposition currents are monitored and the cluster spot is defined by a mask, we know the coverage of Pt atoms on the cluster-containing samples quite accurately (1.5×10^{14} Pt atoms/cm^2). Furthermore, all the Pt and Ge atoms are in the surface layer, where attenuation of the photoelectrons should be negligible, therefore the Pt 4d intensity can be used to put the Pt and Ge coverages on an absolute basis. The ratio of background-subtracted, integrated Ge and Pt XPS intensities (I_{Ge}/I_{Pt}) is related to the coverage ratio X_{Ge}/X_{Pt} as follows:

$$X_{Ge}/X_{Pt} = (I_{Ge}/\sigma_{Ge})/(I_{Pt}/\sigma_{Pt}) \qquad (1)$$

where σ_{Ge} and σ_{Pt} are the Ge 2p and Pt 4d sub-level photoemission cross sections, taken from Yeh and Lindau[1]. The cross section ratio was checked against and agrees well with a ratio derived from the empirical atomic sensitivity factors for our instrument configuration corrected by the ratio of the effective attenuation lengths[2].

It was found that the total amount of Ge deposited for by the $GeCl_4/H_2$/heating treatment on a Pt_4/alumina sample was 13.7 x 10^{13} Ge atoms/cm^2. For a Pt-free alumina sample exposed to the same $GeCl_4/H_2$/heating treatment, the Ge coverage deposited on the alumina support was found to be 9.7 × 10^{13} Ge atoms/cm^2. Because the Pt_4 coverage on Pt_4/alumina was small, it is reasonable to assume that the non-selected Ge deposition on the alumina support was similar in the Pt_4/alumina and alumina samples, and therefore we can estimate the coverage of Ge deposited in association with the Pt_4 clusters to be 4.0 × 10^{13} Ge/cm^2. This is comparable to the density of Pt_4 clusters deposited on the sample, thus the stoichiometry of the clusters is estimated to be $Pt_4Ge_{1.07}$, which is within the uncertainty of Pt_4Ge_1.

The XPS data in these experiments was taken on different days, and has been corrected for variations in the X-ray source intensity or spectrometer sensitivity, using the Al 2s intensity from the alumina support films as a reference. Because the alumina film thicknesses varied slightly between samples, the intensities were also corrected for the alumina thicknesses (determined from the Al 2s: Ta 4d ratio also measured in each spectrum), using the EALs calculated for Al 2s electrons in alumina[2]. Note that this thickness correction was quite small. For example, for typical alumina support film thickness (e.g. 4.7 nm vs. 4.6 nm), the effect of thickness on the Al 2s intensities should be only 0.9%.

Relevant ethane binding modes to Pt_4Ge

Shown in Fig. S3 are typical ethane binding geometries relevant to the C-H activation process when bound to Pt_4Ge/alumina. Only selected isomers are shown since the actual number of binding geometries is large, as can be seen from the small energy differences between the isomers shown.

Pt_4Ge-Ethylene binding modes

Figure S4 shows all the thermally accessible Pt_4Ge ethylene binding modes with their binding energies and Boltzmann populations. Note the abundance of π-binding modes. The structure outlined in red is the one di-σ binding mode which can undertake deeper dehydrogenation.

Acetylene Binding Modes

Figure S5 shows the thermally accessible Pt_4Ge acetylene binding modes. Note the three isomers that contain H dissociated from acetylene, including the global minimum structure. Furthermore, the binding of acetylene seems to induce much more isomerization of the Pt_4Ge core than either ethane or ethylene.

Pt_4C_2/alumina structure

Figure S7 shows the single thermally accessible Pt_4C_2 structure with atomic Bader charges. Note the similarity in shape to the Pt_4GeC_2 structure in Fig 6A. The main difference, however, is the fact that while the overall ΔQ of the cluster is similar to that of Pt_4GeC_2, the charge on the C_2 unit and on the Pt atoms differs significantly from the Pt_4Ge structure, despite the structural similarity.

Gas-phase models of Pt_4C_2 and Pt_4GeC_2

Figure S8 shows the gas-phase models for Pt_4C_2 and Pt_4GeC_2, which were used to derive a Frontier molecular orbital model to describe the change in bonding between Pt_4C_2 and Pt_4GeC_2. We see that the added Ge adopts a formal 2+ oxidation state, and donates the two electrons into the former LUMO of the Pt4C2 system, a π C-C bond, which increases the C-C bonding character of the partially coked cluster.

Pt_4GeC_2 ethane binding modes

Figure S9 shows the low-energy ethane binding modes for the Pt_4GeC_2 cluster. Note that Boltzmann populations have been omitted since the sampling for ethane binding to the cluster is minimal, and we did not want to misrepresent the possible fractions. We did determine that no other Pt atoms seem to act as binding sites for ethane on the Pt_4GeC_2 structure. singlet* indicates that at best guess the cluster was singlet, but some spin contamination was present.

Pt_4GeC_2 ethylene binding modes

Figure S10 shows all the thermally accessible ethylene binding modes identified for the Pt_4GeC_2 cluster. Note the lack of di-σ bonding to adjacent Pt atoms in the ensemble- the only case where we see it is when ethylene also binds to the C2 unit in the center of the Pt_4GeC_2 cluster, but this is a high-energy isomer.

Pt_4GeC_2 C-C cracking end points

Figure S11 shows the C-C cracking endpoints that may be thermodynamically accessible, with the energies relative to the starting points, as well as barrier heights.

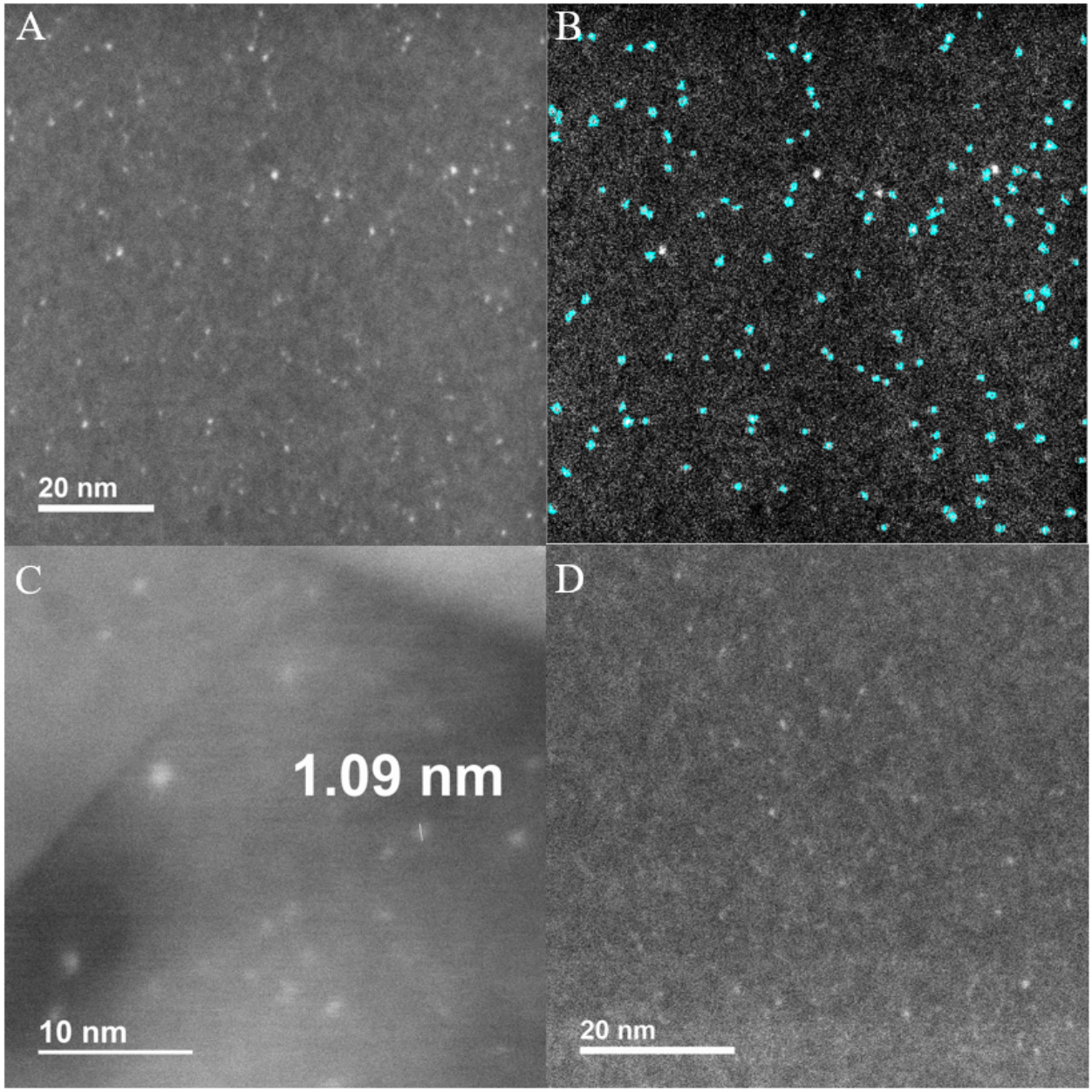

Fig. S1.

(A) S/TEM HAADF Image of 0.01 ML equivalent of Pt_{10} clusters deposited on an ultra-thin carbon film. (B) Image analysis of the cluster coverage of (A). (C) Image of 0.01ML Pt_{10} deposited on a 31 nm thick, oxidized aluminum film grid. (D) Image of 0.01 ML Pt_4 deposited an ultra-thin carbon film grid, showing the absence of any high contrast features that might have formed by sintering.

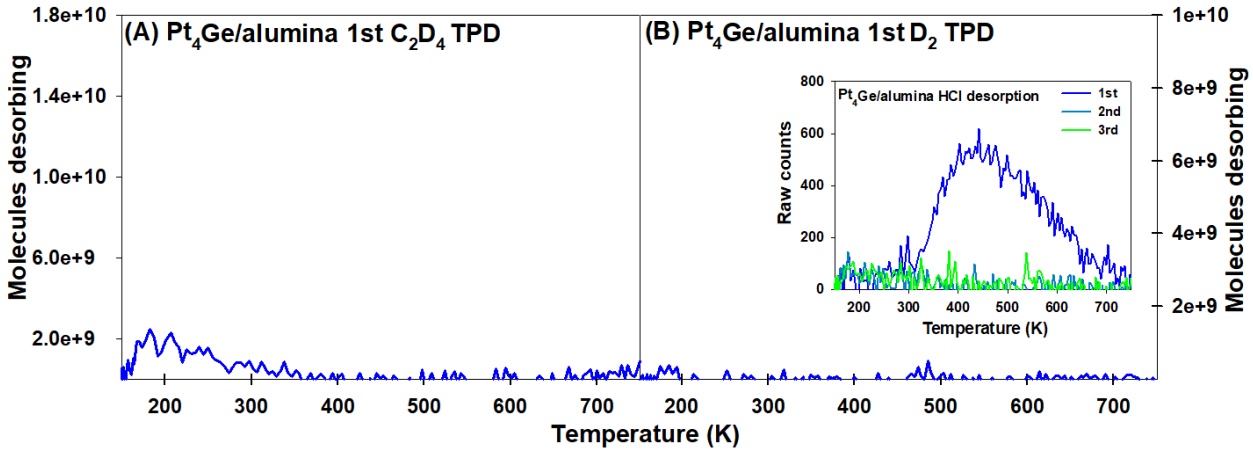

Fig. S2.

TPD measured during the first heating of the Pt_4Ge/alumina sample, under conditions identical to the TPDs shown in Fig. 2 of the main paper. (A) C_2D_4 desorption. (B) D_2 desorption. Inset in (B). Desorption of HCl during the first three TPDs from Pt_4Ge/alumina.

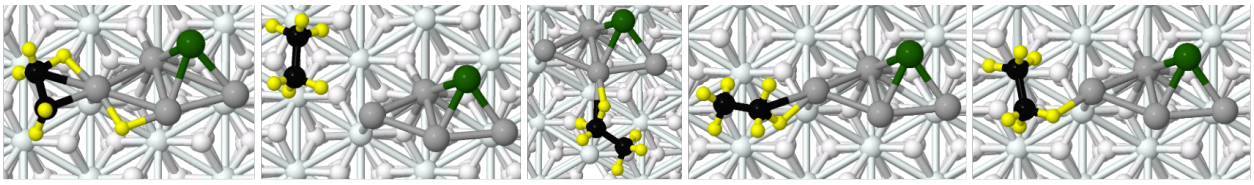

0.0 eV	0.065 eV	0.070 eV	0.082 eV	0.120 eV
BE = -0.66 eV	BE = - 0.59 eV	BE = - 0.58 eV	BE = -0.57 eV	BE = - 0.54 eV
singlet	singlet	singlet	singlet	singlet
C-H = 1.265 Å	C-H = 1.121 Å	C-H = 1.154 Å	C-H = 1.157 Å	C-H = 1.138 Å

Fig. S3.

Key low energy geometries for ethane binding on Pt_4Ge/alumina.

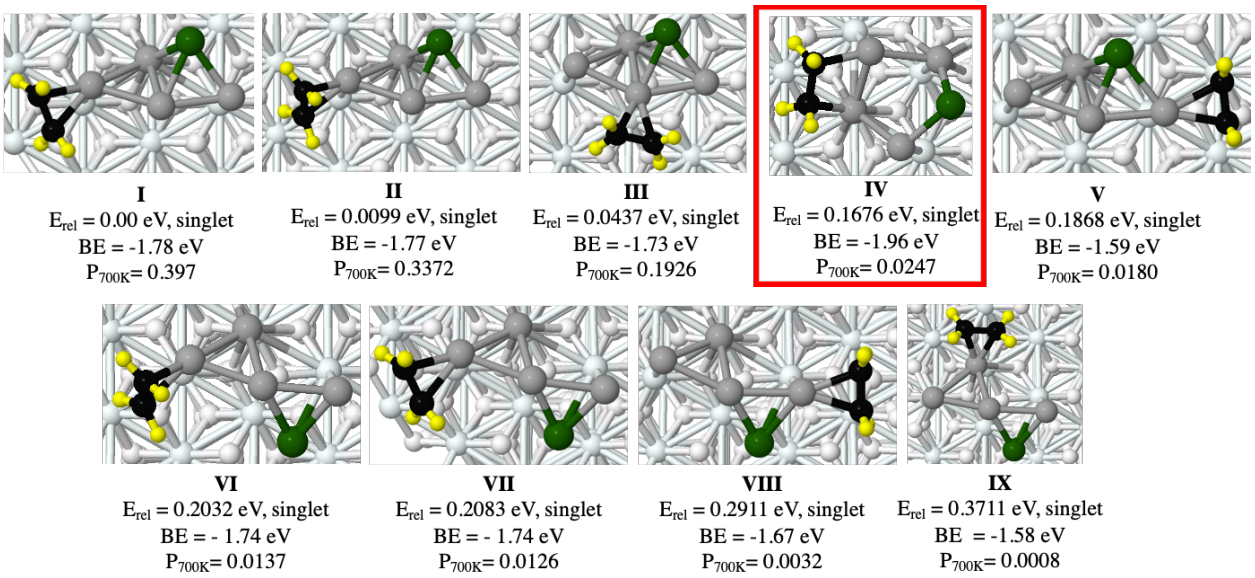

Fig. S4.

All thermally accessible geometries for ethylene binding on Pt_4Ge/alumina.

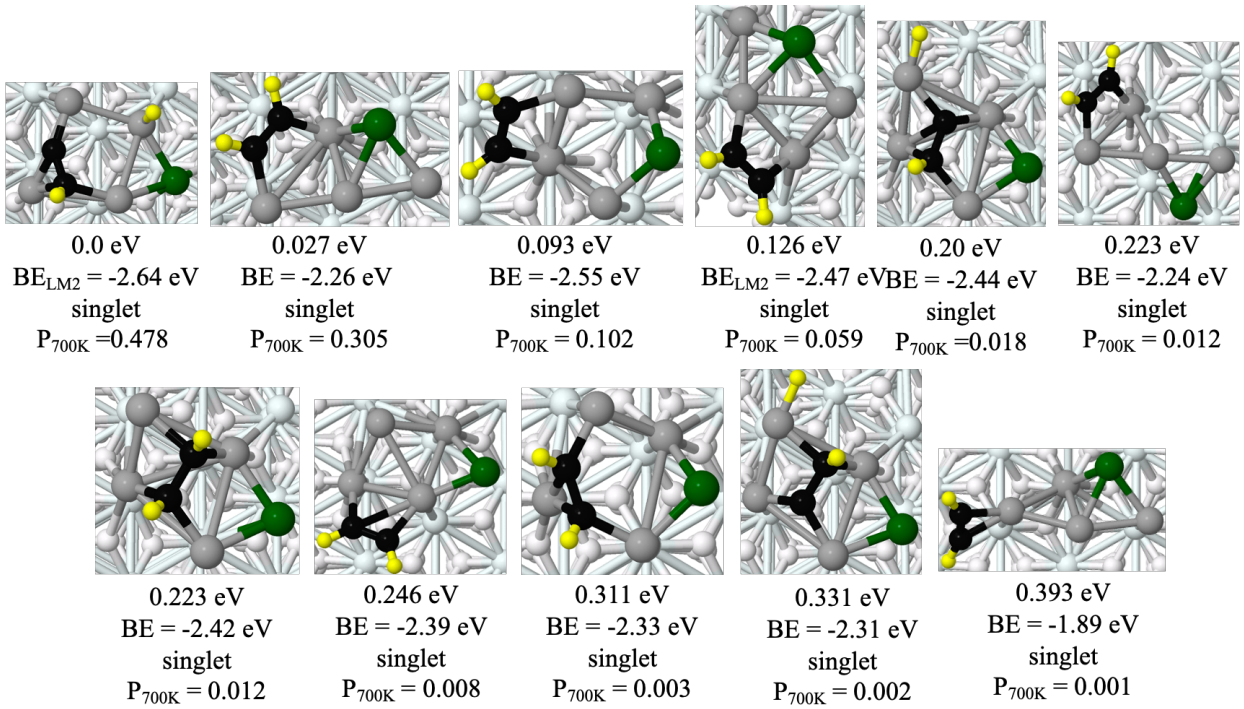

Fig. S5.

All thermally accessible low energy geometries for acetylene binding on Pt_4Ge/alumina.

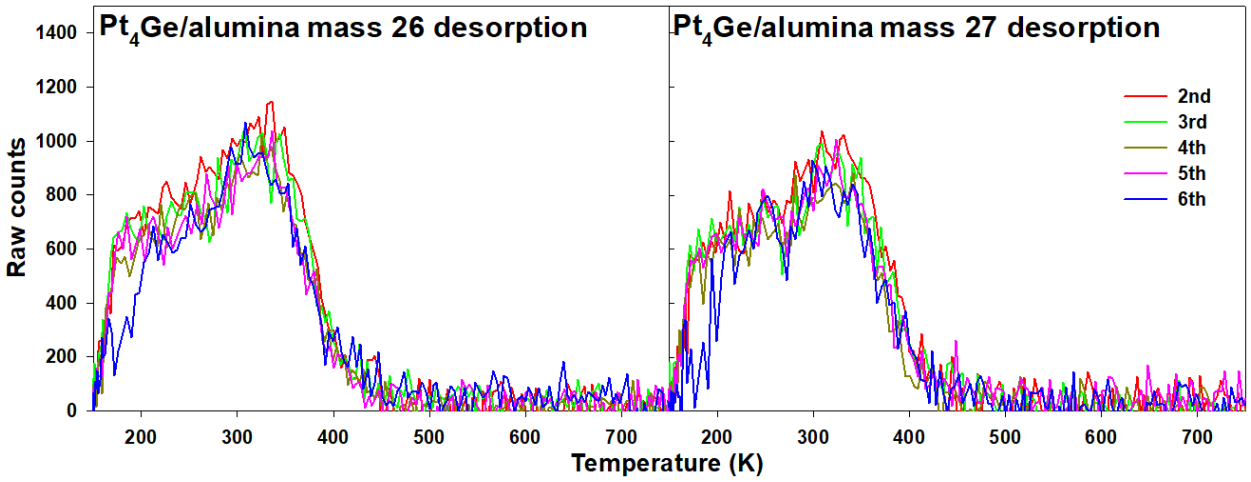

Fig. S6

Mass 26 and 27 from consecutive C_2H_4 TPD experiments of Pt_4Ge/alumina samples. The samples were created and dosed with C_2H_4 exactly the same way as the C_2D_4 TPD experiments in the methods section. C_2H_4 was dosed instead of C_2D_4 due to C_2D_2 mass being 28, which is also the mass of CO. CO has a high background and would greatly interfere with C_2D_2 desorption. Although CO would also interfere with C_2H_4 desorption, fragmentation of C_2H_4 (assuming mass 28 gives 100% signals) from our mass spectrometer results in 67 % mass 26 and 61 % mass 27, hence observing these two mass is adequate for evidence of C_2H_4 desorption. If C_2H_2 desorbs, the majority of the detected mass would be mass 26 and should show up in the mass 26 during TPD experiments; the mass 26 and mass 27 TPD results here are almost identical. With no obvious peaks in mass 26 that distinguish from mass 27, we can conclude no C_2H_2 desorbed off from C_2H_4 dosed Pt_4Ge/alumina samples during TPD experiments.

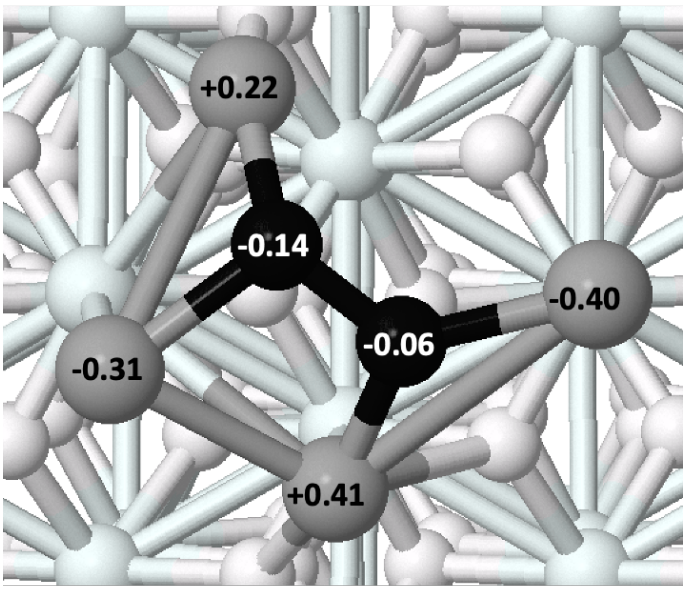

$\Delta Q_{cluster}$ = -0.28 | ΔQ_{Pt} = -0.079 | ΔQ_c= -0.20

Fig. S7.

The structure of Pt_4C_2, with Bader charges shown superimposed on their respective atoms.

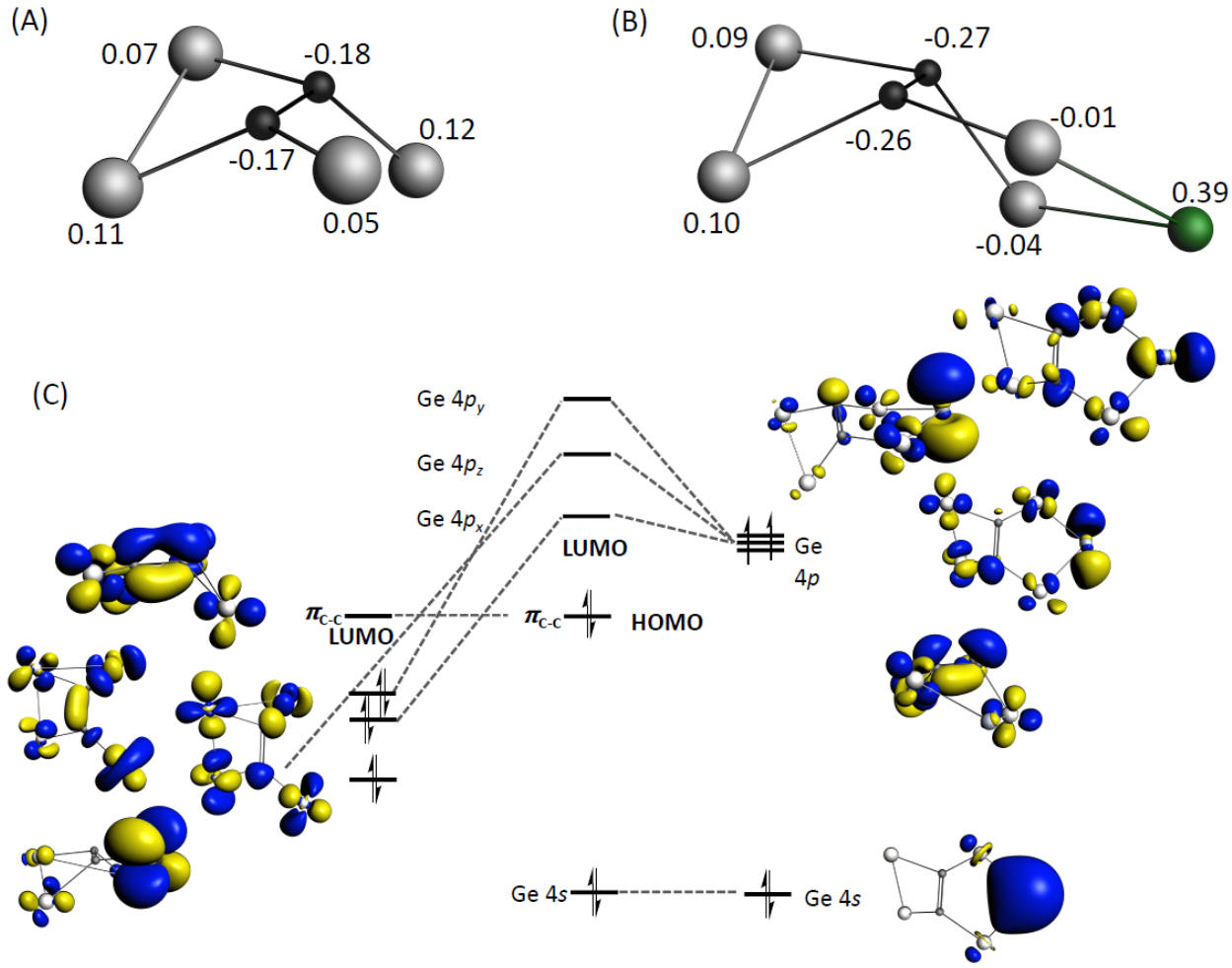

Fig. S8.

The structures of gas-phase models of (A) $Pt_4C_2^-$ and (B) $Pt_4GeC_2^-$ (anionic form due to electron transfer from the alumina support, omitted here) with Bader charges annotated over their respective atoms. (C) The Frontier molecular orbital (MO) diagram showing the interaction of Pt_4C_2 with Ge in $Pt_4GeC_2^-$. Orbitals plotted with an isovalue of 0.06.

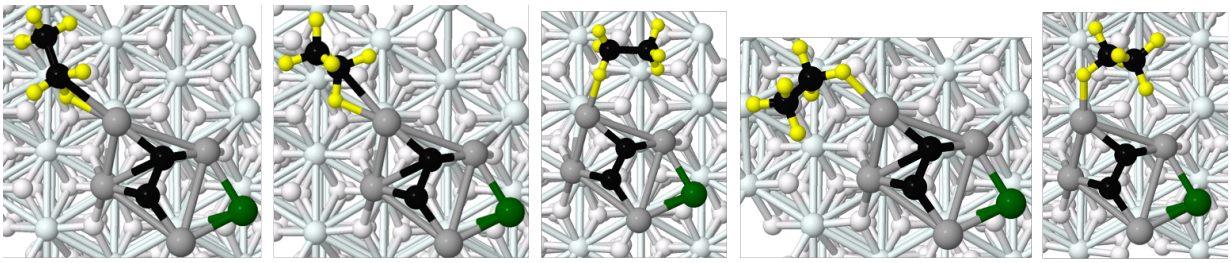

0.0 eV
BE = -0.66
singlet

0. 003 eV
BE = -0.66 eV
singlet

0.063 eV
BE = -0.60 eV
singlet

0.086 eV
BE = -0.57 eV
singlet

0. 123 eV
BE = -0.54 eV
singlet

Fig. S9.

Typical low energy geometries for ethane binding on Pt_4GeC_2/alumina.

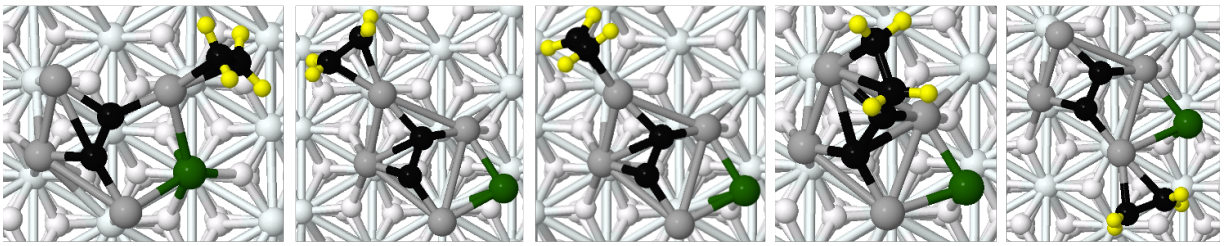

I
ΔE = 0.0 eV, singlet
BE = -1.85 eV

II
ΔE = 0.01 eV, singlet
BE = -1.84 eV

III
ΔE = 0.11 eV, singlet
BE = -1.74 eV

IV
ΔE = 0.33 eV, singlet
BE = -1.52 eV

V
ΔE = 0.33 eV, singlet
BE = -1.51 eV

Fig. S10.

Representative accessible ethylene binding modes for Pt_4GeC_2/alumina.

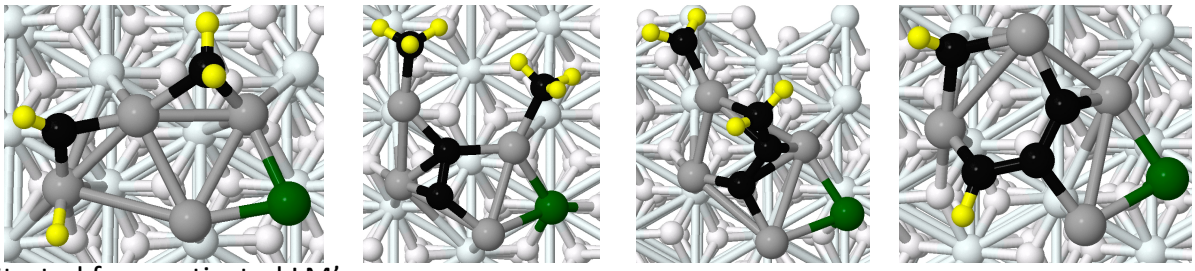

Fig. S11.

Energetically accessible C-C cracking endpoints, with relative energies and reported barriers.

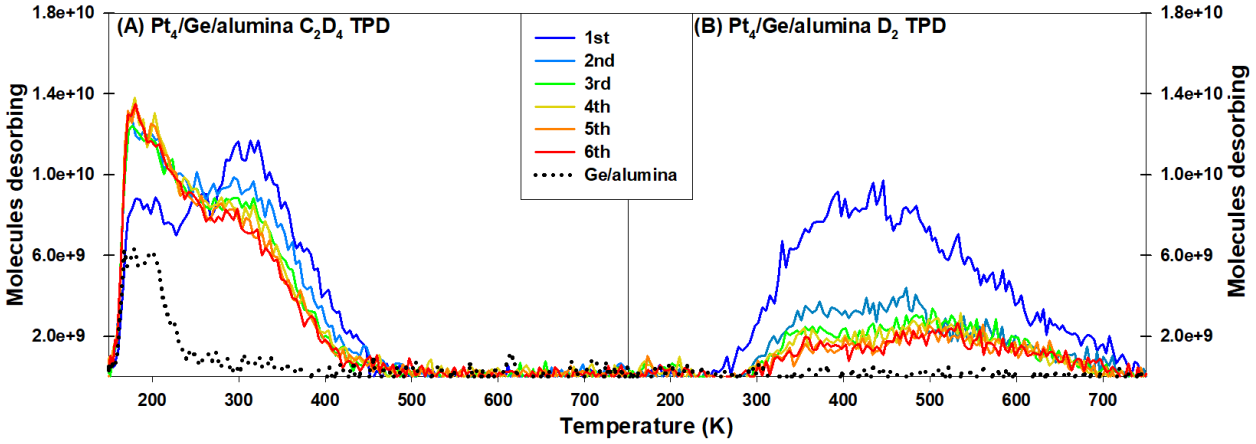

Fig. S12.

TPD results showing (A) C_2D_4 and (B) D_2 desorption from Pt_4 deposited on Ge dosed alumina support.

Table S1.

Desorbing molecule numbers during first 6 TPDs from Pt_4/alumina.

Pt_4 average	**C_2D_4 /cluster**	**D_2 /cluster**	**Total C_2D_4/cluster**	**Accumulated C atoms**
1st	1.63	2.54	2.90	2.54
2nd	1.45	0.98	1.94	3.52
3rd	1.27	0.72	1.63	4.24
4th	1.18	0.58	1.47	4.82
5th	1.07	0.50	1.32	5.32
6th	1.01	0.43	1.23	5.75
Alumina	0.4			

Table S2.

Desorbing molecule numbers during first 6 TPDs from Pt_4Ge/alumina.

Pt_4 average	**C_2D_4 /cluster**	**D_2 /cluster**	**Total C_2D_4/cluster**	**Accumulated C atoms**
1st	N/A	N/A	N/A	N/A
2nd	1.47	0.49	1.71	0.49
3rd	1.47	0.40	1.67	0.89
4th	1.41	0.33	1.57	1.22
5th	1.34	0.30	1.48	1.52
6th	1.32	0.28	1.46	1.79
Alumina	0.38			

References

1 Yeh, J. J. & Lindau, I. Atomic Subshell Photoionization Cross Sections and Asymmetry Parameters: 1< Z < 103. *Atomic Data and Nuclear Data Tables* **32**, 1-155 (1985).

2 NIST Electron Effective-Attenuation-Length Database v. 1.0 (NIST, Gaithersburg, 2001).